EUROPEAN ORGANIZATION FOR NUCLEAR RESEARCH

CERN-EP/89-31
February 14th, 1989

INCLUSIVE PHOTOPRODUCTION OF SINGLE CHARGED PARTICLES AT HIGH P_T

The OMEGA Photon Collaboration

R. J. APSIMON[5], M. ATKINSON[3], M. BAAKE[1], L. S. BAGDASARIAN[7], D. BARBERIS[2], T. J. BRODBECK[4], N. BROOK[3], T. CHARITY[4], A. B. CLEGG[4], P. COYLE[3], S. DANAHER[6], S. DANAGULIAN[7], M. DAVENPORT[2], B. DICKINSON[3], B. DIEKMANN[1], A. DONNACHIE[3], A. T. DOYLE[3], J. EADES[2], R. J. ELLISON[3], P. S. FLOWER[5], J. M. FOSTER[3], W. GALBRAITH[6], P. I. GALUMIAN[7], C. GAPP[1], F. GEBERT[1], G. HALLEWELL[5], K. HEINLOTH[1], R. C. W. HENDERSON[4], M. T. HICKMAN[4], C. HOEGER[1], S. HOLZKAMP[1], R. E. HUGHES-JONES[3], M. IBBOTSON[3], H. P. JAKOB[1], D. JOSEPH[1], N. R. KEEMER[4], J. KINGLER[1], G. KOERSGEN[1], S. D. KOLYA[3], G. D. LAFFERTY[3], H. M^{C}CANN[3], R. M^{C}CLATCHEY[2], C. M^{C}MANUS[3], D. MERCER[3], J. A. G. MORRIS[5], J. V. MORRIS[5], D. NEWTON[4], A. O'CONNOR[4], R. OEDINGEN[1], A. G. OGANESIAN[7], P. J. OTTEWELL[3], C. N. PATERSON[5], E. PAUL[1], D. REID[3], H. ROTSCHEIDT[1], P. H. SHARP[5], S. SOELDNER-REMBOLD[1], N. A. THACKER[6], L. THOMPSON[6], R. J. THOMPSON[3], A. VOIGTLAENDER-TETZNER[1], J. WATERHOUSE[3], A. S. WEIGEND[1], G. W. WILSON[4].

Bonn[1] -CERN[2] -Manchester[3] -Lancaster[4] -RAL[5] -Sheffield[6] -Yerevan[7]

ABSTRACT

Single charged-particle inclusive cross sections for photon, pion and kaon beams on hydrogen at the CERN-SPS are presented as functions of p_T and x_F. Data cover the range $0.0 < p_T < 5.0$ GeV/c and $0.0 < x_F < 1.0$ at incident momenta from 70 to 170 GeV/c. The comparison between photon- and hadron-induced data indicates a relative excess of particles with $p_T > 1.6$ GeV/c for the photon-induced data. Using the hadron-induced data to estimate the hadronic behaviour of the photon, the difference distributions and ratios of cross sections are a measure of the contribution of the point-like photon interactions. The data are compared with QCD calculations and show broadly similar features.

(Submitted to Zeitschrift für Physik C)

Section 1: Introduction.

The relevance of photon-initiated large-p_T processes to the study of QCD has been emphasised repeatedly [1]. Even at a photon-beam energy of $\approx$100 GeV, large-p_T reactions induced by real photons can be a clean and rich source of information on the structure of hadrons and on the dynamics of their constituents. Photon-initiated reactions contain a mixture of hadron-like processes, and a calculable point-like component due to the direct coupling of the photon to the partons. For single-particle inclusive cross sections, the number of processes arising from the point-like component is small. Particularly interesting are the QCD Compton process $\gamma q \rightarrow gq$, the QCD Bethe-Heitler (photon-gluon fusion) process $\gamma g \rightarrow q\bar{q}$ and the higher-twist process $\gamma q \rightarrow Mq$ (where M is a meson). In contrast, the hadron-like processes cannot be calculated reliably in the p_T range being considered.

In this experiment, data were taken with photon, pion and kaon beams using the same experimental set-up. The hadron-beam data were used to estimate the cross section of the hadron-like component of the photon. To do this, it was assumed that the hadronic component of the photon could be represented by an appropriate combination of pion and kaon beams of both charges. At low p_T, this is the well established assumption of Vector Meson Dominance (VMD) combined with the additive quark rule. The ratio between photon- and hadron-induced cross sections is found to be consistent with the expected constancy over a range of p_T and x_F, where it can be assumed that other contributions, for example the point-like photon interactions and leading-particle effects, do not contribute significantly.

Extracting QCD information from photon-induced high-p_T processes is a two-stage process. Firstly, by comparing with the equivalent hadron-induced reactions it is shown that photons do indeed give a different result at high-p_T. Secondly, having established this, measurements are made in the kinematical region where this difference is greatest and where it is reasonable to assume that the point-like interaction of the photon is important.

Photon- and hadron-induced data were taken with the OMEGA Spectrometer at CERN which is well suited for the measurement of complete events. The small fraction of genuine tracks at high p_T makes it necessary to eliminate the occasional fake tracks created by pattern recognition. These effects were studied and rejection algorithms developed using detailed visual inspection of events on a graphics workstation.

This study of inclusive charged particles complements and extends the NA14 results [2] by covering a greater energy range and a wider kinematical region. The results presented here are the first step in a programme to analyse full events at high p_T. The experimental set-up is discussed in section 2, the trigger and normalisation in section 3, and data reduction in section 4. The results and comparison with QCD are presented in section 5 and there is a brief summary in section 6.

Section 2: The Experiment.

The data reported in this paper were taken by the WA69 collaboration using the CERN Omega spectrometer. The beamline, shown in fig 1(a), was used to transport particles of momenta of up to 200 GeV/c through a spectrometer with three identical detector systems

(referred to as regions 1, 2 and 3 on fig 1(a)) consisting of four scintillator hodoscopes and four planes of MWPCs. Individual beam particles could be recognised unambiguously by the series of scintillator hodoscopes and measured with a typical momentum accuracy of 250 MeV/c by the MWPCs. The beamline was used either with electrons as a source of tagged photons or with hadrons.

In the tagged-photon mode, a flux of 7×10^6 electrons per SPS pulse (of 2.8 s duration) was produced which yielded $\approx 7\times10^5$ bremsstrahlung photons in a 9% radiation-length tagging radiator. Electrons which lost no energy were bent by magnets and were absorbed by a lead wall at the entrance to Omega. The scattered electrons in the momentum range 130 to 20 GeV/c, corresponding to bremsstrahlung photons between $\approx$ 65 and 175 GeV/c, entered the tagging system, shown in fig 1(b), where the momentum of the photon was measured to better than 0.5%. The tagging system consisted of a series of MWPCs (W4.1-4.6), two scintillator hodoscope arrays (H4.1-4.2) and a lead-glass array (LG) which allowed incident electrons to be identified.

In the hadron mode, the same beamline was used to derive a collimated flux of 6×10^4 positive or negative particles at momenta of either 80 GeV/c or 140 GeV/c, within momentum windows of $\pm$0.25%. In addition to the detectors which measured the momentum of the incident beam, two beam Čerenkov counters (CEDARs) were incorporated in order to identify kaons and pions.

A 600mm long liquid-hydrogen target was positioned within the Omega spectrometer which was set up in the standard way, with MWPCs used for stereoscopic reconstruction of tracks (see fig 2). The A chambers each had three planes with wire orientations at 0° and $\pm$ 10.14° from the vertical, while each B and C chamber had 2 planes with wire orientations alternating between 0°, +10.14° and 0°, −10.14° for successive chambers. A high-precision wire chamber (HPC) with 0.5mm pitch provided accurate measurements within an 8 x 8cm square immediately downstream of the hydrogen target. The two lever-arm drift chambers, situated outside the field, were 150cm high and 320cm wide and used four sense planes (with wires at 0°, $\pm$10.14° and 0°) to provide a typical hit accuracy of 0.18mm for particles with momenta above $\approx$ 5 GeV/c. To the rear of Omega was a RICH (Ring-Image Čerenkov detector) which was used to provide particle identification for the outgoing pions, kaons and protons [3]. This was capable of providing pion/kaon discrimination from 5 to 80 GeV/c and kaon/proton discrimination from 20 to 160 GeV/c. Two trigger hodoscope arrays were used; H1 was situated directly in front of the RICH with H4 behind it. Further downstream was a transition-radiation detector used to provide particle identification for charged tracks with momenta above 70 GeV/c [4].

Neutral particles were detected in electromagnetic calorimeters. In this analysis their use was confined to the removal, in the trigger, of e^+ e^- pairs from the photon data. The Outer Photon Detector was constructed in four quadrants, each with three segments in depth and has been described previously [5]. The Inner Calorimeter in the centre of the outer photon detector consisted of 165 units in a 13 by 13 array with the four central units missing. The units were 3.2cm square and 31cm deep and were each connected to a photomultiplier tube. They were made up of 1mm diameter scintillating optical fibres sandwiched between crinkled layers of 1mm lead sheet oriented parallel to the beam axis.

The furthest downstream of the WA69 detectors was the beam-veto counter used to correct the photon momentum given by the tagging system in cases where double bremsstrahlung occurred and also used to veto events in the trigger where the energy deposition exceeded 30 GeV. It consisted of 54 layers of 16cm square 2mm thick lead alternating with 6mm scintillator sheets, corresponding to approximately 20 radiation lengths. Light produced by the shower was collected by 12 wavelength-shifting BBQ lightguides and detected by 24 photomultiplier tubes mounted at either end of the detector.

Section 3: Trigger and Normalisation.

For photons, the cross section for pair production is approximately 20 mb compared with 115 μb for the total hadronic cross section. This small hadronic cross section, combined with the available flux of photons, meant that the trigger could select all hadronic events produced in the hydrogen target. This open trigger did not saturate the data-acquisition system and could be used for a wide range of photon-induced hadronic physics. The trigger requirement had to be as similar as possible for tagged-photon and hadron beams since comparisons were to be made. However, because of the differing beam particles, the trigger requirements were necessarily different in defining a beam particle for the two cases.

The trigger was in stages so that an event could be rejected as early as possible, thus minimising dead time. The initial beam trigger corresponded to a beam particle entering Omega and interacting in the hydrogen target. For photon data, an electron radiating a photon at the tagging target and being 'tagged' was signalled by a three-fold coincidence between the two hodoscope arrays and the lead glass array. Background in the tagging system was reduced by using the radiation veto (fig 1(b)) to reject events where bremsstrahlung, or an excessive amount of synchrotron radiation, had been produced in the latter parts of the beamline. The two 'holey' vetoes (HOV1 and HOV2) situated on either side of the lead shielding wall in front of Omega served to collimate the photon beam. Signals from the scintillators (S2 and V2) in the beamline just in front of Omega were used to reject events where the photon had converted downstream of the tagging magnets. In the case of the hadron beam, the beam trigger consisted of a coincidence between signals from scintillators in the beam in region 3 with the tagging target counter shown in fig 1(a). The fraction of kaon-induced interactions was enhanced to $\approx 25\%$ of all main triggers using signals from the pion and kaon CEDARs.

A signal from a scintillation counter (endcap) immediately downstream of the hydrogen target was used to indicate an interaction in the hydrogen target for the photon data. The endcap was also incorporated into the hadron-data trigger in order to reduce any differences due to the selection biasses of the endcap counter.

The remainder of the trigger was designed to select hadronic interactions using the trigger elements shown in fig 3. The opening angle of the electrons and positrons from the dominant 'pairs' events in the case of photon-induced data is negligibly small and the distribution of pairs away from the median plane was effectively determined by the phase space of the incident beam. The charged beam was therefore focussed vertically approximately half way between H1 and H4, and the upper and lower parts of H1 and H4 were adjusted so that almost all pairs and the photon/hadron beam passed between them. The H1 scintillator

hodoscope consisted of 32 slats above and 32 slats below the the median plane with a gap between them of ±2.5cm. The H4 hodoscope consisted of 15 slats above and 15 below the median plane with a ±3.5cm separation. A matrix coincidence was required between specific slats of H1 and H4 to signal that at least one charged particle had passed through the system. This matrix was set to accept all reasonable charged-particle trajectories from hadronic interactions which emanated from the hydrogen target. This same matrix coincidence was used to define an interaction for hadron-induced data. The suppression of scattered electromagnetic pairs was assisted by a veto from the median plane of the outer photon detector in conjunction with the neighbouring sections of the inner calorimeter. The combined effect of all the above triggers on photon data was to suppress the remaining electromagnetic events to less than 30% of all triggered events whilst preserving an almost unbiassed open hadronic trigger.

The total number of photon-induced events was approximately 20 million over the momentum range $65 < p_\gamma < 175$ GeV/c. A similar total number of hadron-induced events, divided approximately equally between both charges, was accumulated at beam momenta of 80 and 140 GeV/c, for comparison purposes.

The absolute normalisation of the data was achieved using direct counting of beamline tagged photons or charged particles throughout the data-taking periods. For the photon-beam data, the background due to soft photons was a potential problem. The soft photons, however, did not generally achieve the requirements of a trigger in the tagging system. Another source of uncertainty resulted from the effect of the beam-veto rejecting events. This occurred mainly when the interacting photon was accompanied by a secondary bremsstrahlung photon of energy greater than 30 GeV. There was also a small effect due to self-vetoing by very forward π^os. Monitor triggers were used to quantify these effects. For the photon-beam data, the systematic error in the measurement of the beam flux was estimated at ±15% compared with ±10% for the hadron-beam data.

All trigger-counter efficiencies were incorporated in a full Monte Carlo simulation of the apparatus which could be used to find the overall acceptance for any specific type of event. Typical counter efficiencies were greater than 95%. The trigger-counter inefficiencies and the geometrical acceptance of H1 and H4 were such that more than 85% of hadronic events were triggered. The loss depended on the charged multiplicity of the events and weakly on the x_F of the charged particles but was insensitive to their p_T. The effects of track-finding inefficiencies were small.

Section 4: Data Reduction.

The Omega measurements were analysed with the program TRIDENT [6] to find and fit tracks and determine the event vertex. All events which did not belong to the main trigger or where the photon momentum was outside the tagging range were discarded. Events were only accepted if the reconstructed interaction vertex was inside the hydrogen-target. Residual electromagnetic interactions were removed by eliminating events where all tracks were within a dip of ±4 mrad relative to the beam. Elastic events (i.e. ρ^o, ω, ϕ for the photon-beam data and single charged particles for the hadron-beam data) were biassed by the trigger and were different for photon and hadron beams. Hence a software cut was

applied for both photon- and hadron-induced data to low charged multiplicity events. For the photon-beam data, a cut of $x_F > 0.9$ for the combination of the two most forward particles was applied to two- or three-track events. This corresponded to the exclusion of the elastic production of ρ^o and ϕ mesons. For the hadron-beam data, a cut of $x_F > 0.9$ for a single charged particle was applied to one or two track events.

As the interest was in the extraction of a relatively small signal (of high-p_T tracks), the performance of TRIDENT was critical and it has been upgraded to improve pattern recognition efficiency and error calculations. After the standard pattern recognition was completed, TRIDENT scanned all chambers to attach any hit which could belong to a track. This procedure was important for the linking of drift-chamber digitisings to the upstream part of a track where track finding could be confused by the high track density. The success of pattern recognition in TRIDENT depended critically on the tolerances used in the geometrical reconstruction. The optimisation was a compromise between finding tracks with wrongly associated digitisings (tolerances too loose) and the loss of track information resulting from correct digitisings being omitted (tolerances too tight). Simulated events were used to tune and measure the performance of TRIDENT. The events were generated by the Lund program LUCIFER [7] according to the lowest-order photon-induced QCD processes, with subsequent fragmentation into hadronic multi-particle final states according to JETSET [8]. The final particles were traced through the Omega system using OMGEANT [9]. This produced digitisings smeared according to the observed experimental resolution and simulated the background.

Pattern recognition problems were found to be due to -

mis-associated digitisings from confusion between closely spaced tracks, occurring mostly at the upstream end of the tracks,

mis-associated digitisings from incoherent background being combined with track segments of true secondaries, and

digitisings from the incoherent background being combined into spurious tracks.

These problems were heavily suppressed by retaining only tracks with reasonably well-measured momentum. Hence, tracks were required to have 5 or more space points fitted to them. Since the dominant contribution to the error on p_T is the $1/p$ error term (i.e. $\sigma(p_T)/p_T \approx \sigma(p)/p = p \cdot \sigma(1/p)$), the distributions of $\sigma(1/p)$ were studied. Fig 4 shows $\log_{10}\sigma(1/p)$ distributions for all tracks with positive x_F. The structure seen in fig 4 is due to the nature of the Omega detector. The peaks correspond to tracks with almost all MWPC space points and, from left to right, with space points from

2 drift chambers and the HPC (2.0×10^{-4} $(GeV/c)^{-1}$);

2 drift chambers and no HPC *or* 1 drift chamber and the HPC (4.5×10^{-4} $(GeV/c)^{-1}$);

no drift chamber and the HPC (1.3×10^{-3} $(GeV/c)^{-1}$); and

neither drift chamber nor HPC (4.0×10^{-3} $(GeV/c)^{-1}$).

A similar distribution, with peaks at the same positions, was found by reconstructing tracks from simulated events.

An error on p_T of less than ≈ 0.2 GeV/c is needed to make satisfactory measurements of p_T distributions. This was satisfied for all selected tracks with $p < 10$ GeV/c and for tracks with momenta in the range 10 GeV/c $< p <$ 100 GeV/c only when drift-chamber points were attached. The error requirement has been achieved by two alternative approaches.

One method was based on the errors of the relevant track parameters $(1/p, \lambda, \varphi)$ obtained from the simulation and reconstruction program. As discussed above, the magnitude of the errors depended on the number of chambers hit by the track. This led to a classification of tracks according to the set of chambers traversed. Sensible error cuts for each class have been extracted from these distributions and subsequently applied to the real data. The simulation showed that the cuts did not bias the p_T distributions.

The other method did not rely on observed track errors nor simulation but simply required that tracks with $p > 10$ GeV/c, which intersected the drift-chambers, must have drift-chamber points. This eliminated most fake high-p_T tracks and did not discard preferentially high-p_T tracks intersecting the chambers at relatively large angles. The effect of this cut was to reduce the total number of genuine tracks with momenta above 10 GeV/c by $\approx 15\%$ in a way that did not bias the p_T distributions.

In each case corrections were applied in order to remove the x_F biasses produced by the cuts. The two methods selected almost the same tracks and yielded the same final p_T and x_F distributions, well within statistical errors.

Since the large-p_T region is of particular interest, visual scanning techniques were applied to high-p_T candidate tracks. These showed that, with the above cuts applied, there was still a contamination of tracks with mis-associated points (normally in the upstream part of the track). These tracks had a closest distance to the measured vertex well outside the error tolerance of the vertex fit. Hence a loose cut on the absolute distance of closest approach of the extrapolated track to the vertex was used. The cut also removed fake high-p_T tracks which originated from interactions upstream of the target. Visual inspection verified that genuine large-p_T tracks were not rejected by the cut and that contamination was now small even at the highest p_T measured in the experiment.

Nuclear interactions of produced particles in the target or chamber material could, in principle, be a source of fake high-p_T tracks. The amount of contamination when a single track was reconstructed using digitisings partly from a primary vertex track and partly from a secondary track has been investigated by Monte Carlo calculations. The problem arose when the original track and a high momentum secondary track were of the opposite sign. Since the transverse momentum was calculated at the primary vertex, this gave an additional p_T which, even when the momentum was correctly measured, was up to twice the p_T given to a particle by the magnetic field between the primary and secondary vertices. After cuts, these effects were largest for a small class of interactions in the later A chambers and corresponded to an apparent p_T of up to 2.0 GeV/c. In practice the apparent momentum could also be raised, increasing the p_T above 2.0 GeV/c. These secondary interaction effects within Omega were approximately the same for hadron- and photon-induced data. Monte Carlo studies, using measured inclusive charge-exchange cross sections [10], however, showed that the probability of these events was very small and distorted the individual

p_T distributions by a negligible amount.

Global checks of the performance of the data reduction are provided by:

i) The correlation between original and reconstructed p_T values of tracks from simulated events (shown in fig 5(a)). The acceptance losses introduced by the software are shown on fig 5(b) and are independent of p_T. Thus the level of creation of fake p_T values and the level of losses caused by the software are both small.

ii) The angular distribution around the beam of samples of tracks with a $p_T > 2.0$ GeV/c (shown in fig 6) before and after the cleaning procedures described above. The magnetic field and the small stereo angle of the Omega chambers both create an asymmetry for fake high-p_T tracks and before cleaning this was very pronounced (fig 6(a)). The fact that these distributions are flat after cleaning (fig 6(b)) indicates that the sample in this p_T range is dominated by well-measured tracks and that the angular acceptance for real high-p_T tracks is flat.

The overall acceptance in p_T has been shown by Monte Carlo studies to be essentially the same as the software acceptance shown in fig 5. In x_F, the acceptance is flat for $0.0 < x_F < 0.7$ and decreases as x_F approaches 1.0.

Section 5: Results.

Photon-induced data were selected within two incident momentum bins, from 70 to 90 GeV/c and 110 to 170 GeV/c. These ranges were chosen to match the momenta of the hadron beams (80 GeV/c and 140 GeV/c). Differential cross sections of single-inclusive charged particles in terms of x_F and p_T, for photon-beam data in the momentum range 110 - 170 GeV/c and for the 140 GeV/c pion and kaon beam data, are shown in table 1. The p_T- and x_F- dependences and normalisation of the hadron-beam data are within the range of previous results (for references see Adamus et al [11]).

The differential cross sections are shown in figs 7 and 8 as functions of p_T and x_F respectively. In fig 7 integration is over all $x_F > 0.0$ while on fig 8 integration is over all $p_T > 2.0$ GeV/c. The photon differential cross sections are shown as solid circles while the hadron differential cross sections, divided by a VDM factor of 215, are shown as open circles. The hadron-beam data were weighted so as to contain approximately the same strange to non-strange quark fraction as that expected for the photon. This corresponds to 40% kaon-induced events and 60% pion-induced events. The results were not, however, sensitive to this fraction in the kinematical region of this study.

The ratio of photon-beam differential cross sections to hadron-beam differential cross sections on a bin by bin basis is shown on fig 9. Tracks with $p_T < 0.3$ GeV/c are excluded in order to remove a small residual electromagnetic contamination from the photon data. Four major features are clear:

a) An approximately flat region with $0.3 < p_T < 1.0$ GeV/c and $0.0 < x_F < 0.6$ over which the ratio varies by less than 15%. This flat behaviour is as expected from simple VMD arguments.

b) A constant ratio across most of the p_T range at x_F close to 0, as one approaches the

target fragmentation region.

c) A rapid decrease at large x_F over all p_T. At low p_T this would be expected because of differing leading particle effects – hadron beams produce single leading particles, while photons give vector mesons whose decay products share longitudinal momentum and hence deplete the single-particle inclusive cross section at large x_F. The extension of this phenomenon to large-p_T, also shown in fig 8 as a relative excess of high-x_F tracks in the hadron beam data, is a surprising feature.

d) A rise at large p_T, particularly at medium x_F, which can be ascribed to QCD processes.

Following a) above, the hadron-beam data have been normalised to give a ratio of 1.0 over this flat region. This choice of normalisation region minimises problems due to differing leading-particle effects on the one hand and QCD effects on the other. There are, however, residual variations in the ratio over this region and these lead to a systematic normalisation error of $\pm 10\%$. The normalisation factor for the hadron-beam data, with an associated error due to luminosity uncertainties, is $1/(215\pm30)$. This result compares with the usual factor of $1/(201\pm13)$ obtained from ratios of total cross sections for photons and pions [12]. Following c) above, only $x_F < 0.7$ is considered in the subsequent analysis. In fact the contribution at high x_F is unimportant for the integrated p_T spectra.

The general features of the data shown on fig 9 are quantified by projections of the ratio. These are shown in fig 10 as a function of p_T, integrated over $0.0 < x_F < 0.7$, and in fig 11 as a function of x_F, integrated over all $p_T > 2.0$ GeV/c. The normalisation is as discussed above.

To compare the data with QCD predictions of the point-like interaction of the photon, two alternative approaches have been used for the QCD calculations:

a lowest-order calculation of minimum twist and higher twist in which events are generated by the Lund Monte Carlo LUCIFER, and

a second-order calculation using independent fragmentation and applying the principle of minimum sensitivity to specify the scale factor in α_s; the anomalous structure function of the photon can be included in this calculation [1].

In principle, the second approach fixes the absolute magnitude of the cross section, unlike the lowest-order calculation where the normalisation is essentially arbitrary, depending on an effective Λ_{QCD}.

If the higher-twist contribution is switched off in the LUCIFER calculation, and if the contribution of the anomalous structure function of the photon is switched off in the higher-order calculation then the two approaches give almost the same shapes for the p_T and x_F distributions. At this level, the first-order calculation is normalised to the second-order one with an effective $\Lambda_{QCD} \simeq 300$ MeV (which is, in fact, the default LUCIFER value). The set 1 structure functions of Duke and Owens [13] are used for the second-order calculation and those of Eichten et al. [14] are used for LUCIFER.

Figs 12 and 13 show the results of subtracting the hadron data (normalised as discussed above) from the photon data. This is a measure of the point-like component of the photon

interaction (assuming there is no interference between the contributions to the cross section). The distributions have, where appropriate, been corrected for acceptance variations. The subtractions have been done on a bin by bin basis. For $p_T > 1.6$ GeV/c, the uncertainty in the relative normalisation of the photon and hadron data is sufficiently small for meaningful subtractions to be made. The p_T distributions are shown in fig 12, integrated over x_F from 0.0 to 0.7 for $p_T > 1.6$ GeV/c. Fig 13 shows the corresponding x_F distributions integrated over $p_T > 2.0$ GeV/c. These cross sections are a direct measure of the QCD-calculable contribution from the point-like interaction of the real photon and the results of both QCD calculations are shown superimposed on the data.

Figs 12 and 13 show general agreement between the data and the theoretical predictions. The small difference in overall normalisation between the data and the higher-order calculation of Aurenche et al. is not significant. The only discrepancy of any consequence between the data and the QCD calculations is in the shape of the x_F distributions. This discrepancy is apparent at low x_F and at the higher beam momentum, and originates primarily from tracks with p_T close to the cut at 2.0 GeV/c, a relatively low p_T. This is a region where perturbative QCD is generally less reliable and which is sensitive to a poorly known part of the gluon structure function. The discrepancy is greater when the anomalous structure function of the photon is included in the calculation. This, of course, is one of the least certain parts of the calculation, and the anomalous structure function of the photon has been the subject of much study in γ-γ reactions and of much debate (see for example [15]). An additional possibility is that interference effects between the various contributions to the total cross section may not be negligible.

Section 6: Conclusions.

Single charged-particle inclusive cross sections from photon- and hadron-beams have been measured. A key element in this experiment was the use of the same detector set-up, the same trigger and the same software for both the photon- and hadron-beam data. The results justify the assumption that, over a wide range of p_T and x_F, the hadron-like contribution of the photon is given by the scaled hadron-beam data, which is an extension of the usual VMD argument from low p_T to high p_T. It has been confirmed that for $p_T > 1.6$ GeV/c there is an additional contribution to the photon cross section.

The predictions of QCD, describing the point-like interaction of the real photon, give a good description of the broad features of the additional contribution to the photon cross section for $p_T > 2.0$ GeV/c and $0.0 < x_F < 0.7$. Detailed differences are observed in the x_F distributions which may be due to the inherent uncertainty of perturbative QCD-based predictions in parts of the kinematic region studied, or to interference effects between the contributions to the photon cross section.

ACKNOWLEDGEMENTS.

We are most grateful to G. Ingelman who developed LUCIFER and helped us to apply it to our experiment, and to M. Fontannaz, P. Aurenche and co-workers who modified their program to compare with our data. This assistance was invaluable.

BMFT -Foerderkennzeichen 05-4BN14P(0) (Fed. Rep. Germany) and SERC (U.K.) helped financially and we gratefully acknowledge this. All our technicians, the CERN OMEGA and beam line groups made vital contributions and to them and CERN generally we are indebted for the success of our work.

The computer centres (RHRZ at Bonn, RAL, and CERN) have been most generous in their support and we are most grateful to them.

REFERENCES.

[1] P. Aurenche et al., Nucl. Phys. B286 (1987) 553, and references contained therein.

[2] E. Auge et al., Phys. Lett. 168B (1986) 163, and
R. Barate et al., Phys. Lett. 174B (1986) 458.

[3] R. J. Apsimon et al., NIM A248 (1986) 76, and RAL-83-047.

[4] S. Holzkamp, PhD Dissertation, University of Bonn (1988), and
G. Koersgen, PhD Dissertation, University of Bonn (1988).

[5] M.Bonesini et al., NIM A261 (1987) 471.

[6] J.C. Lassalle et al., CERN-DD/EE/79-2, and NIM 176 (1980) 371.

[7] G. Ingelman and A. Weigend, DESY report 87-018 (1987), and
CERN pool program W5047 Long write-up (1986).

[8] T. Sjöstrand, Comp. Phys. Comm. 39 (1986) 347.

[9] F. Carena and J.C. Lassalle, CERN-DD/EE/79-1.

[10] F.Pauß et al., ACCMOR Collaboration, Zeit. Phys. C27 (1985) 211.

[11] M. Adamus et al., EHS-NA22 Collaboration, Zeit. Phys. C39 (1988) 311.

[12] Particle Data Group, Phys. Lett. 170B (1986).

[13] D. W. Duke and J. F. Owens, Phys. Rev. D26 (1982) 1600, D28 (1983) 1227.

[14] E. Eichten et al., Rev. Mod. Phys. 56 (1984) 579.

[15] J. H. Da Luz Vieira and J. K. Storrow, Phys. Lett. B205 (1988) 367.

[16] M. Fontannaz, private communication.

FIGURE CAPTIONS.

fig 1 (a) The beamline spectrometer.

(b) The tagging system used with the photon beam.

fig 2 Plan view of the WA69 apparatus including the Omega system.

fig 3 The WA69 trigger elements.

fig 4 Omega spectrometer resolution: $\log_{10} \sigma(1/p)$ distributions for all tracks with positive x_F. The arrows refer to the Omega measurements discussed in the text.

fig 5 (a) The correlation between original and reconstructed p_T values of selected tracks from simulated events.

(b) The software acceptance as a function of p_T.

fig 6 The angular distribution around the beam of tracks with $p_T > 2.0$ GeV/c, for

(a) a small sample of unselected tracks, and

(b) a much larger sample of selected tracks.

fig 7 Single-particle cross sections as a function of p_T, integrated over x_F from 0.0 to 1.0. The full circles (•) correspond to photon-beam data, and open circles (o) to the corresponding hadron-beam data scaled as described in the text. The hadron data are for fixed momenta centred on the photon momentum ranges.

fig 8 Single-particle cross sections as a function of x_F, integrated over $p_T > 2.0$ GeV/c. The full and open circles have the same meaning as in fig 7.

fig 9 The ratio of photon-beam data to normalised hadron-beam data for the higher incident momentum range. Bins, at high p_T and x_F, with statistical errors greater than 30% have been set to zero.

fig 10 The ratio of the cross sections for the photon data to normalised hadron data as a function of p_T, integrated over x_F from 0.0 to 0.7.

fig 11 The ratio of the cross sections for the photon data to normalised hadron data as a function of x_F, integrated over $p_T > 2.0$ GeV/c.

fig 12 The subtracted p_T distributions, integrated over x_F from 0.0 to 0.7, for $p_T > 1.6$ GeV/c. The data, indicated by •, are shown with the combined statistical errors of the photon and hadron data. The systematic error in the normalisation of the photon and hadron data of $\pm 10\%$ propagates to the errors indicated by the horizontal lines. An additional normalisation error of $\pm 15\%$ is not shown.
The superimposed curves show the second-order QCD prediction of Aurenche et al. [1]. The full line corresponds to the prediction of the second-order calculation of the point-like coupling. The dashed line includes this point-like contribution and a term due to the anomalous photon coupling. The $\triangle$ points indicate the LUCIFER Monte Carlo prediction including minimum and higher twist.

fig 13 The subtracted x_F distributions integrated over $p_T > 2.0$ GeV/c. The points and curves are as for fig 12. The LUCIFER higher-twist contribution is significant for the lower-momentum range and is responsible for most of the difference between LUCIFER and the Aurenche et al. point-like coupling contribution. The result of the calculation including the anomalous photon component has been omitted at low x_F as it is unreliable in that kinematic region [16].

P_T (GeV/c)	X_F 0.0 - 0.2	0.2 - 0.4	0.4 - 0.6	0.6 - 0.8	0.8 - 1.0
	$d^2\sigma/dx_F.dp_T$ for 110 - 170 GeV γ data (nb/GeV/c)				
0.0-0.4	$(2.37 \pm 0.01)10^6$	$(2.60 \pm 0.01)10^5$	$(8.48 \pm 0.03)10^4$	$(3.59 \pm 0.02)10^4$	$(1.61 \pm 0.01)10^4$
0.4-0.8	$(8.28 \pm 0.01)10^5$	$(2.26 \pm 0.01)10^5$	$(8.00 \pm 0.03)10^4$	$(2.76 \pm 0.02)10^4$	$(4.86 \pm 0.07)10^3$
0.8-1.2	$(1.21 \pm 0.01)10^5$	$(5.22 \pm 0.02)10^4$	$(2.26 \pm 0.02)10^4$	$(9.04 \pm 0.09)10^3$	$(1.57 \pm 0.04)10^3$
1.2-1.6	$(1.77 \pm 0.01)10^4$	$(9.25 \pm 0.09)10^3$	$(4.51 \pm 0.06)10^3$	$(1.69 \pm 0.04)10^3$	$(3.0 \pm 0.2)10^2$
1.6-2.0	$(3.09 \pm 0.05)10^3$	$(1.94 \pm 0.04)10^3$	$(9.8 \pm 0.3)10^2$	$(3.6 \pm 0.2)10^2$	$(4.6 \pm 0.7)10^1$
2.0-2.4	$(5.8 \pm 0.2)10^2$	$(4.2 \pm 0.2)10^2$	$(2.4 \pm 0.1)10^2$	$(8.0 \pm 0.7)10^1$	$(2.0 \pm 0.4)10^1$
2.4-2.8	$(1.3 \pm 0.1)10^2$	$(1.2 \pm 0.9)10^2$	$(6.5 \pm 0.7)10^1$	$(1.9 \pm 0.4)10^1$	$(5 \pm 2)10^0$
2.8-3.2	$(3.0 \pm 0.4)10^1$	$(2.6 \pm 0.4)10^1$	$(1.7 \pm 0.3)10^1$	$(4 \pm 2)10^0$	$(1.6 \pm 1.0)10^0$
3.2-3.6	$(8.4 \pm 2.4)10^0$	$(9.7 \pm 2.5)10^0$	$(5.4 \pm 1.9)10^0$	$(1.5 \pm 1.0)10^0$	$(1.6 \pm 1.0)10^0$
3.6-4.0	$(3.7 \pm 1.6)10^0$	$(2.6 \pm 1.3)10^0$	$(2.7 \pm 1.3)10^0$	$(6 \pm 6)10^{-1}$	$(6 \pm 6)10^{-1}$
	$d^2\sigma/dx_F.dp_T$ for 140 GeV $\pi^\pm$ data (nb/GeV/c)				
0.0-0.4	$(5.06 \pm 0.01)10^8$	$(5.13 \pm 0.01)10^7$	$(1.52 \pm 0.01)10^7$	$(8.35 \pm 0.02)10^6$	$(3.37 \pm 0.02)10^6$
0.4-0.8	$(1.96 \pm 0.01)10^8$	$(5.17 \pm 0.01)10^7$	$(1.62 \pm 0.01)10^7$	$(6.37 \pm 0.02)10^6$	$(2.32 \pm 0.01)10^6$
0.8-1.2	$(2.86 \pm 0.01)10^7$	$(1.18 \pm 0.01)10^7$	$(4.88 \pm 0.02)10^6$	$(1.78 \pm 0.01)10^6$	$(6.31 \pm 0.07)10^5$
1.2-1.6	$(4.07 \pm 0.02)10^6$	$(1.92 \pm 0.01)10^6$	$(8.48 \pm 0.08)10^5$	$(3.49 \pm 0.05)10^5$	$(1.46 \pm 0.03)10^5$
1.6-2.0	$(6.38 \pm 0.07)10^5$	$(3.43 \pm 0.05)10^5$	$(1.48 \pm 0.03)10^5$	$(6.4 \pm 0.2)10^4$	$(2.7 \pm 0.1)10^4$
2.0-2.4	$(1.15 \pm 0.03)10^5$	$(6.4 \pm 0.2)10^4$	$(2.9 \pm 0.1)10^4$	$(1.2 \pm 0.9)10^4$	$(7.6 \pm 0.7)10^3$
2.4-2.8	$(2.1 \pm 0.1)10^4$	$(1.4 \pm 0.1)10^4$	$(7.0 \pm 0.7)10^3$	$(2.6 \pm 0.4)10^3$	$(1.4 \pm 0.3)10^3$
2.8-3.2	$(4.7 \pm 0.6)10^3$	$(2.4 \pm 0.4)10^3$	$(1.6 \pm 0.3)10^3$	$(5.7 \pm 2.0)10^2$	$(6.3 \pm 2.1)10^2$
3.2-3.6	$(8.6 \pm 2.4)10^2$	$(8.6 \pm 2.4)10^2$	$(5.7 \pm 2.0)10^2$	$(5.1 \pm 1.9)10^2$	$(1.2 \pm 0.9)10^2$
3.6-4.0	$(1.7 \pm 1.1)10^2$		$(1.1 \pm 0.9)10^2$	$(6 \pm 6)10^1$	
	$d^2\sigma/dx_F.dp_T$ for 140 GeV $K^\pm$ data (nb/GeV/c)				
0.0-0.4	$(4.40 \pm 0.01)10^8$	$(4.67 \pm 0.01)10^7$	$(1.25 \pm 0.01)10^7$	$(5.11 \pm 0.03)10^6$	$(2.08 \pm 0.02)10^6$
0.4-0.8	$(1.75 \pm 0.01)10^8$	$(4.50 \pm 0.01)10^7$	$(1.35 \pm 0.01)10^7$	$(4.95 \pm 0.03)10^6$	$(1.78 \pm 0.02)10^6$
0.8-1.2	$(2.63 \pm 0.01)10^7$	$(1.09 \pm 0.01)10^7$	$(4.33 \pm 0.03)10^6$	$(1.67 \pm 0.02)10^6$	$(6.70 \pm 0.12)10^5$
1.2-1.6	$(3.87 \pm 0.03)10^6$	$(1.85 \pm 0.02)10^6$	$(8.39 \pm 0.14)10^5$	$(3.54 \pm 0.09)10^5$	$(1.71 \pm 0.06)10^5$
1.6-2.0	$(6.10 \pm 0.12)10^5$	$(3.35 \pm 0.09)10^5$	$(1.48 \pm 0.06)10^5$	$(6.6 \pm 0.4)10^4$	$(3.8 \pm 0.3)10^4$
2.0-2.4	$(1.11 \pm 0.05)10^5$	$(6.9 \pm 0.4)10^4$	$(3.0 \pm 0.3)10^4$	$(1.6 \pm 0.2)10^4$	$(7.7 \pm 1.3)10^3$
2.4-2.8	$(2.2 \pm 0.2)10^4$	$(1.6 \pm 0.2)10^4$	$(6.2 \pm 1.2)10^3$	$(4.3 \pm 1.0)10^3$	$(7 \pm 4)10^2$
2.8-3.2	$(5.6 \pm 1.1)10^3$	$(2.4 \pm 0.8)10^3$	$(1.3 \pm 0.6)10^3$	$(1.0 \pm 0.5)10^3$	$(4 \pm 3)10^2$
3.2-3.6	$(8 \pm 4)10^2$	$(1.1 \pm 0.5)10^3$			$(2 \pm 2)10^2$
3.6-4.0		$(8 \pm 4)10^2$			

Table 1 Photon and hadron cross sections for the higher energy data.
The errors shown are statistical only, the photon (hadron) data has a normalisation uncertainty of ± 15% (± 10%).

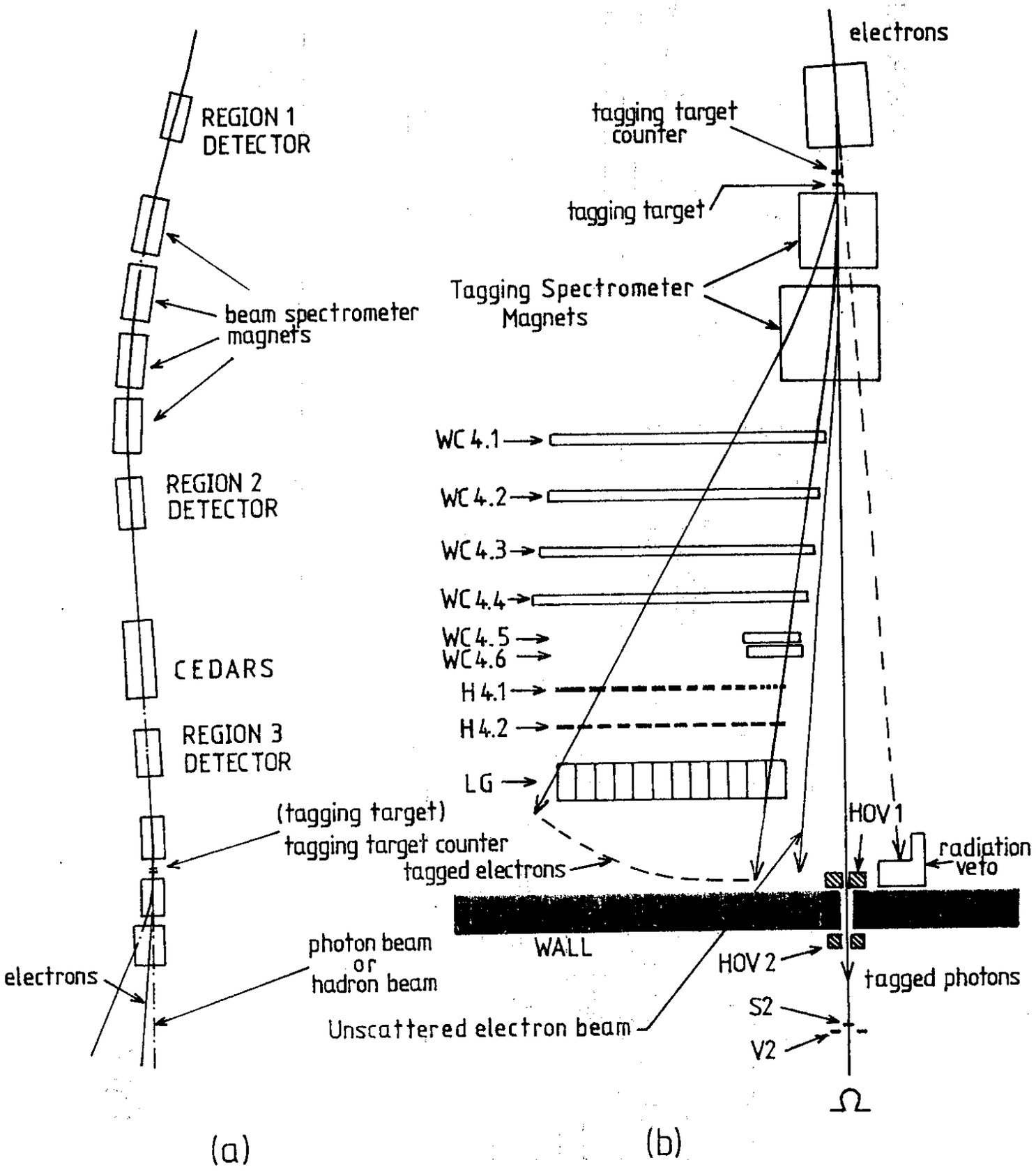
REGION 1
DETECTOR
beam spectrometer
magnets
REGION 2
DETECTOR
CEDARS
REGION 3
DETECTOR
(tagging target)
tagging target counter
electrons
photon beam
or
hadron beam
(a)
electrons
tagging target
counter
tagging target
Tagging Spectrometer
Magnets
WC 4.1
WC 4.2
WC 4.3
WC 4.4
WC 4.5
WC 4.6
H 4.1
H 4.2
LG
tagged electrons
HOV 1
radiation
veto
WALL
HOV 2
tagged photons
S2
V2
Unscattered electron beam
Ω
(b)

Fig.1

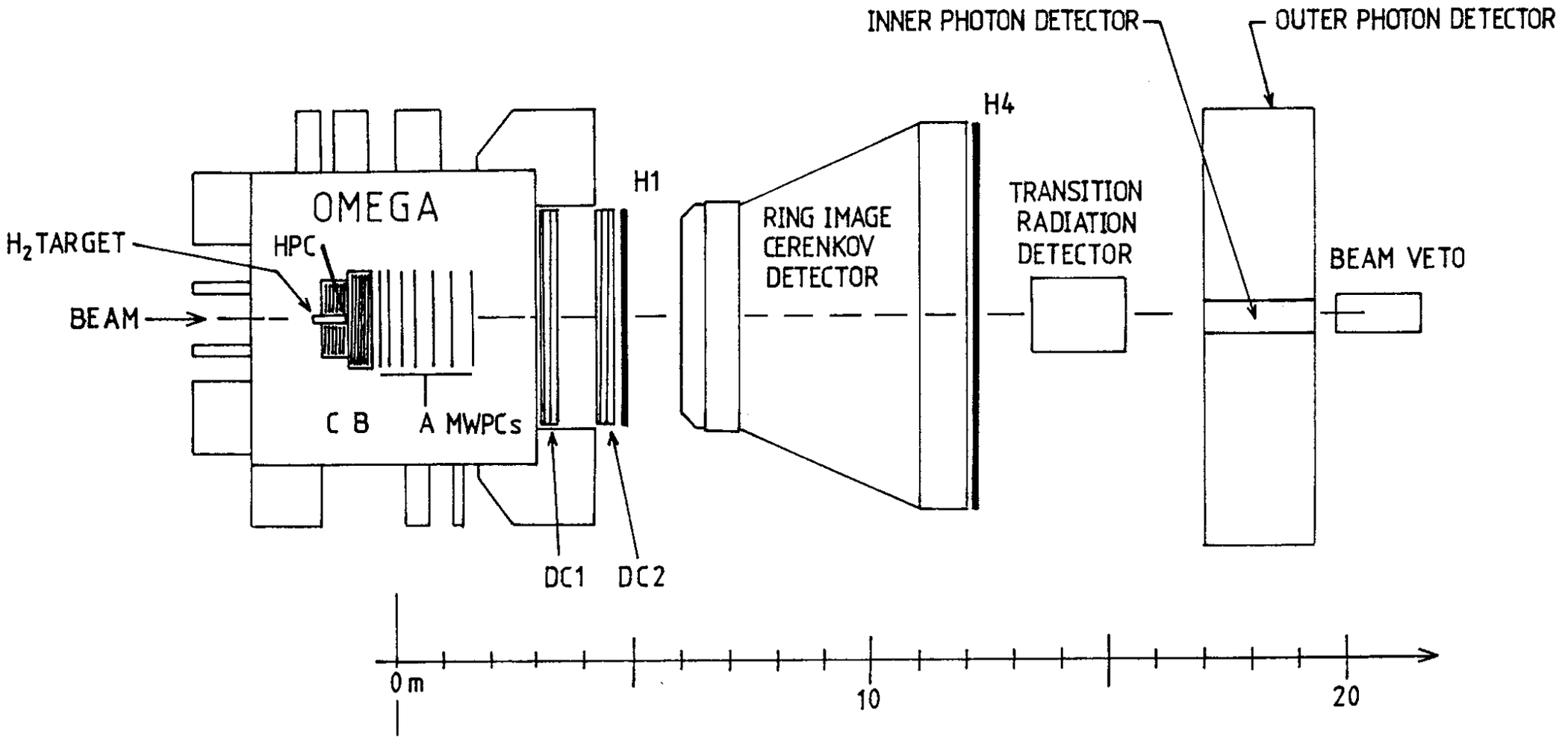
INNER PHOTON DETECTOR
OUTER PHOTON DETECTOR
H4
H1
OMEGA
H_2 TARGET
HPC
BEAM
RING IMAGE CERENKOV DETECTOR
TRANSITION RADIATION DETECTOR
BEAM VETO
C B
A MWPCs
DC1
DC2
0 m
10
20

Fig. 2

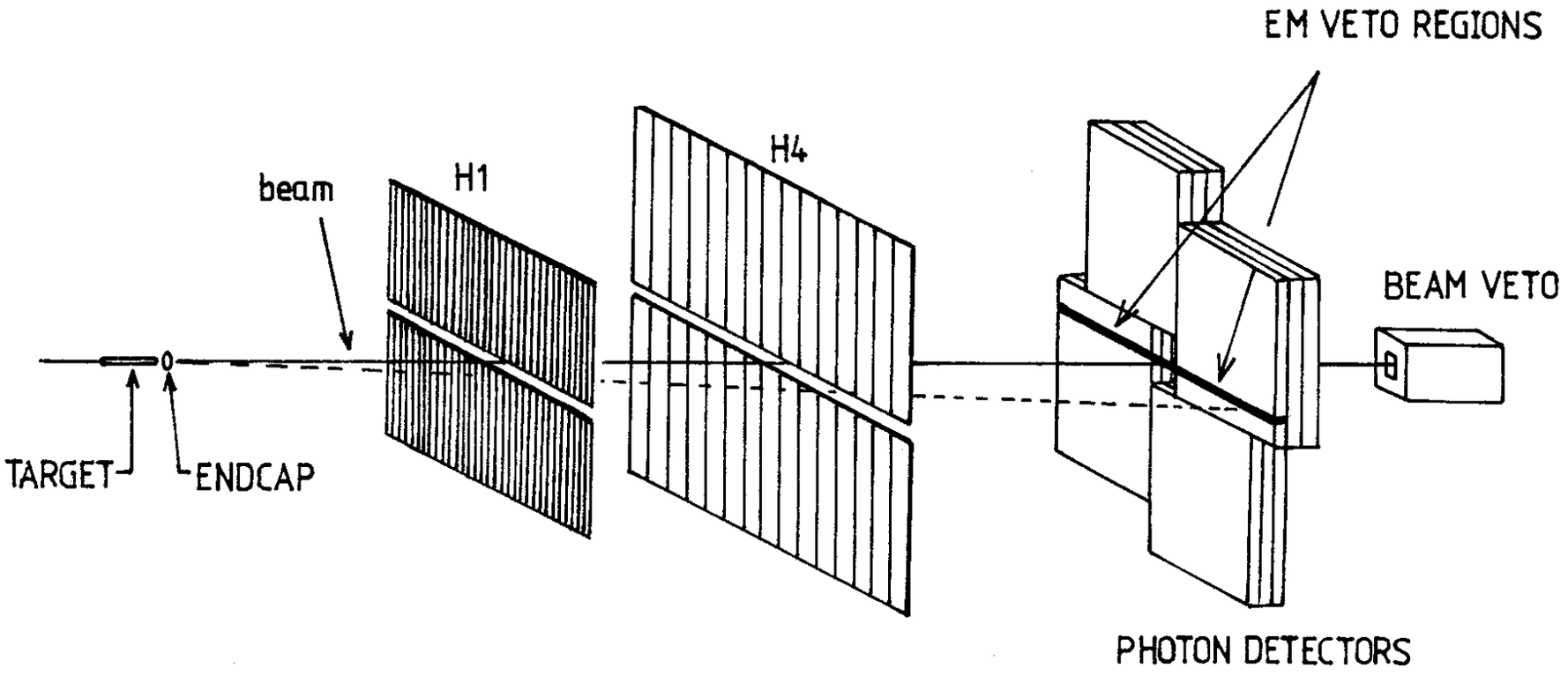
EM VETO REGIONS
beam
H1
H4
BEAM VETO
TARGET
ENDCAP
PHOTON DETECTORS

Fig. 3

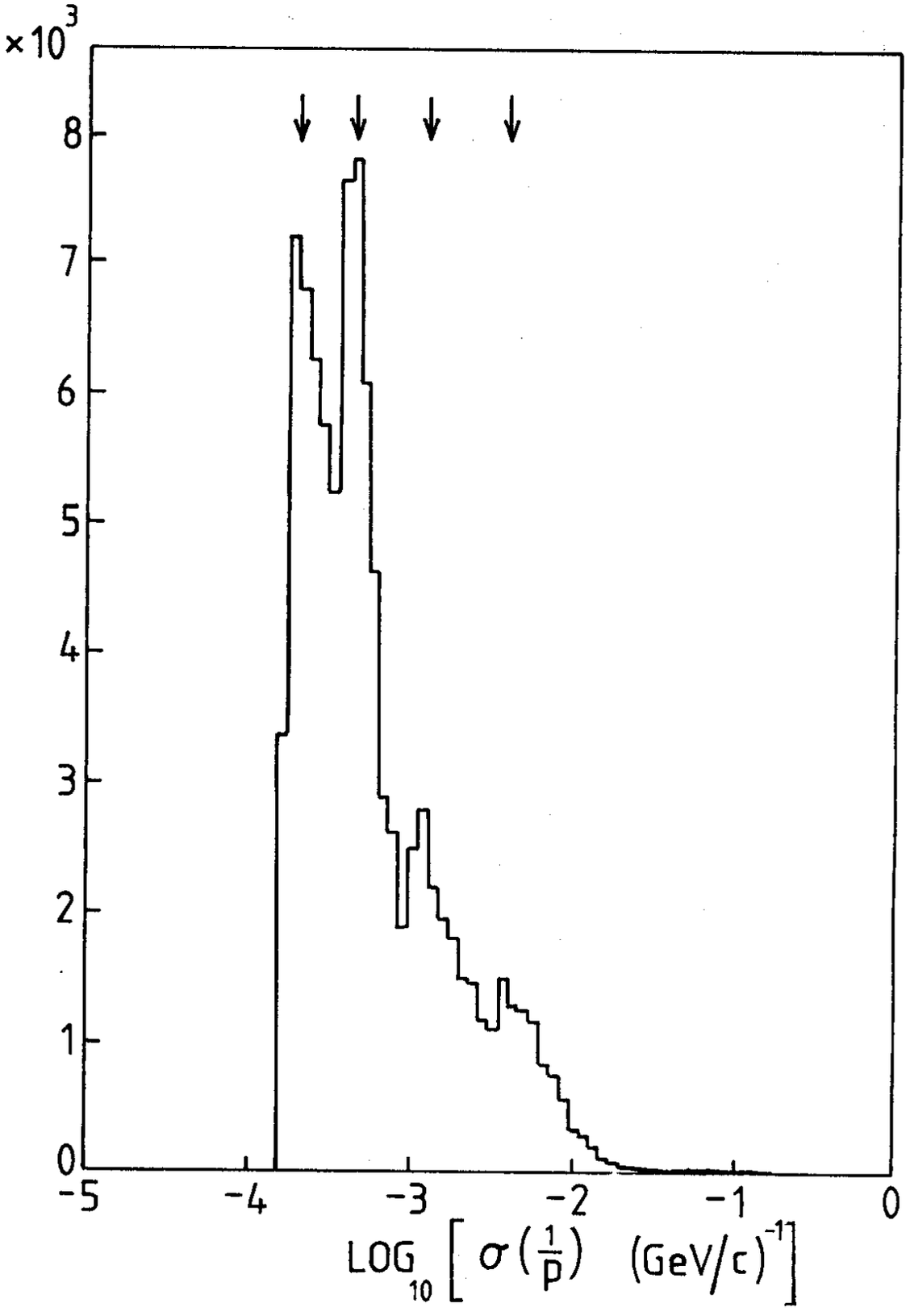

Fig. 4

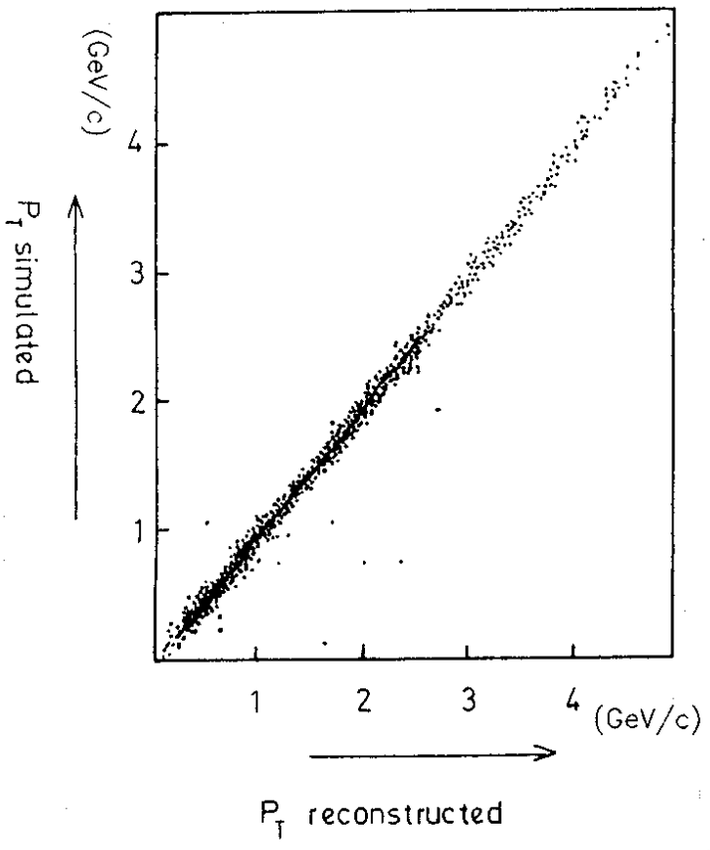
(GeV/c)
4
3
2
1
P_T simulated
1
2
3
4
(GeV/c)
P_T reconstructed

(a)

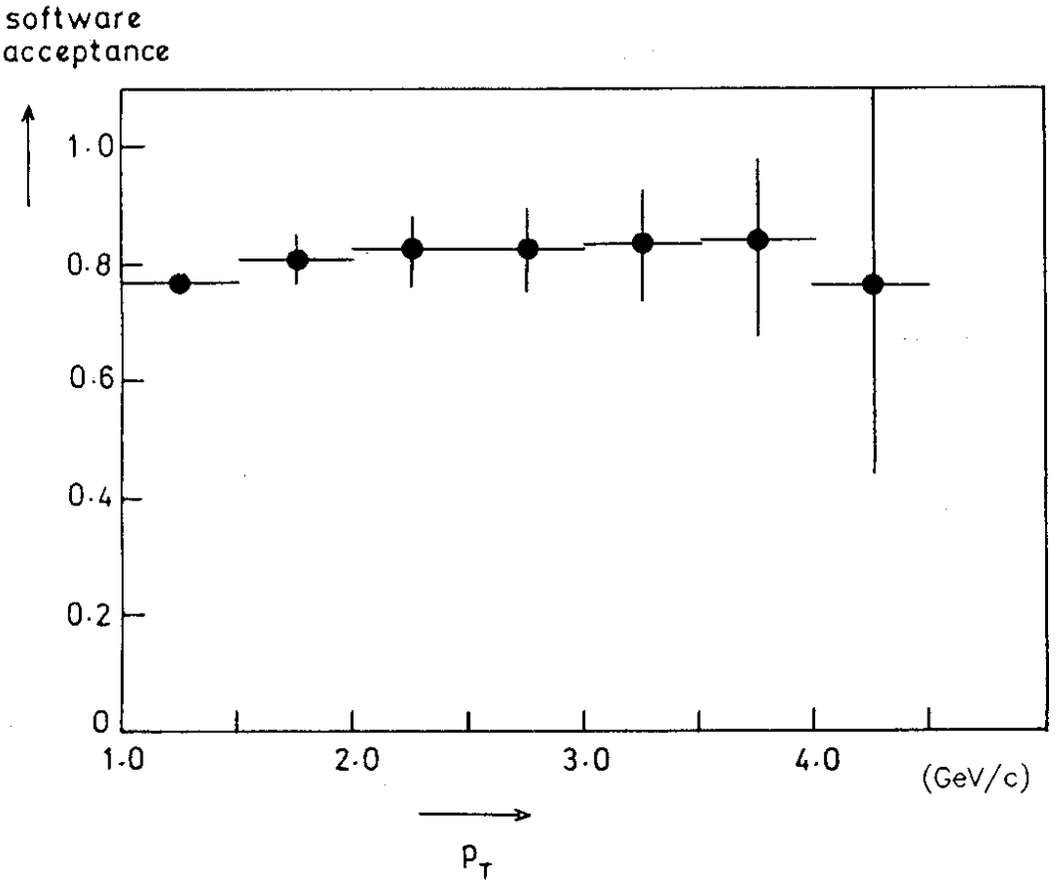
software
acceptance
1·0
0·8
0·6
0·4
0·2
0
1·0
2·0
3·0
4·0
(GeV/c)
P_T

(b)

fig 5

fig 6

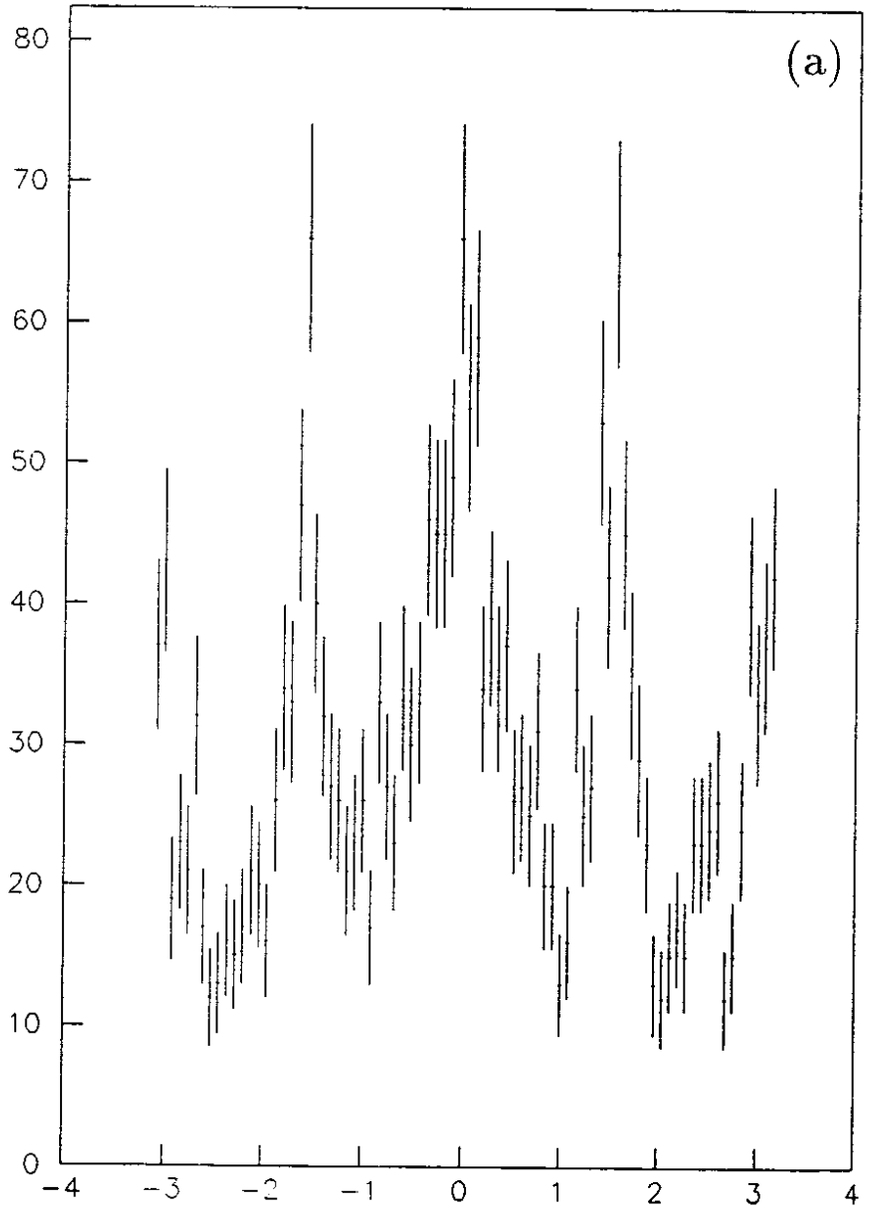

Φ distribution: original p_T>2.0 GeV/c tracks [radians]

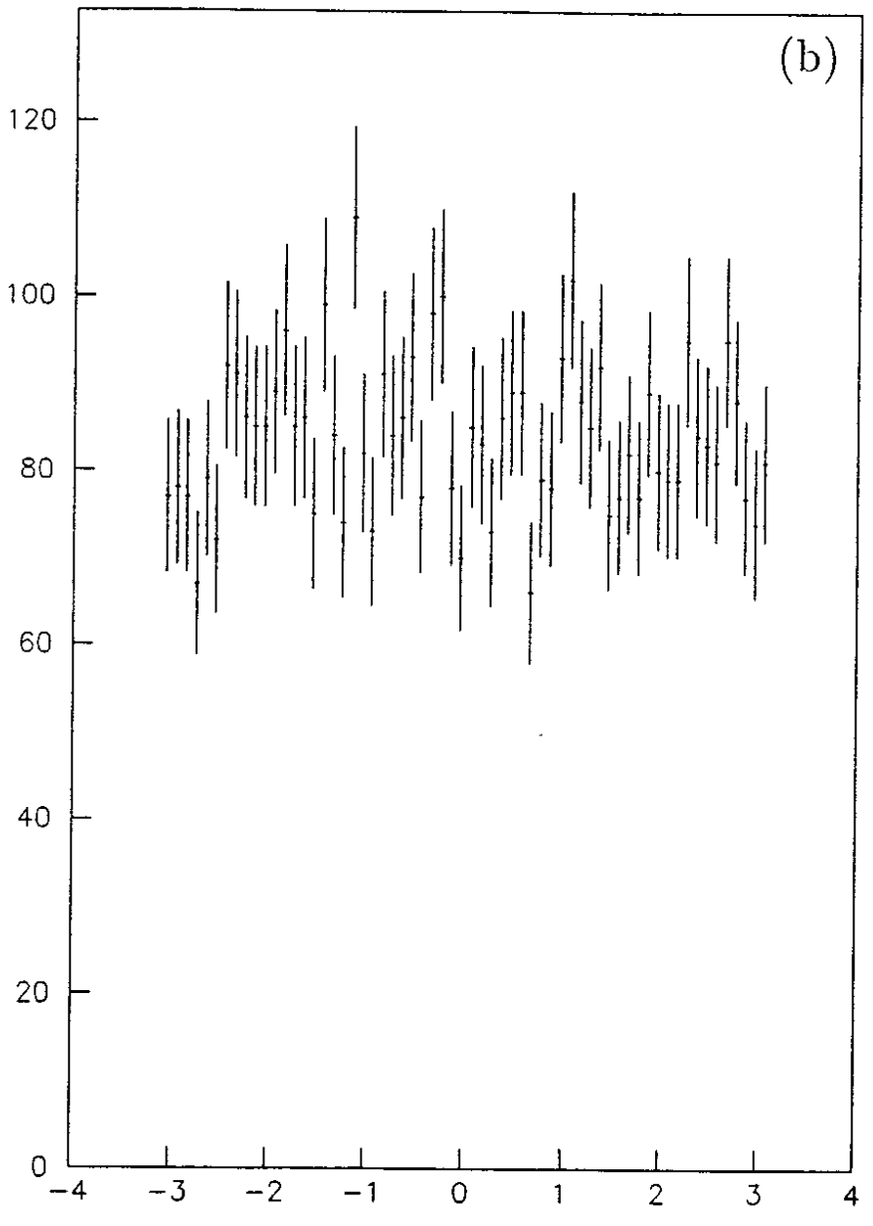

Φ distribution: selected p_T>2.0 GeV/c tracks [radians]

fig 7

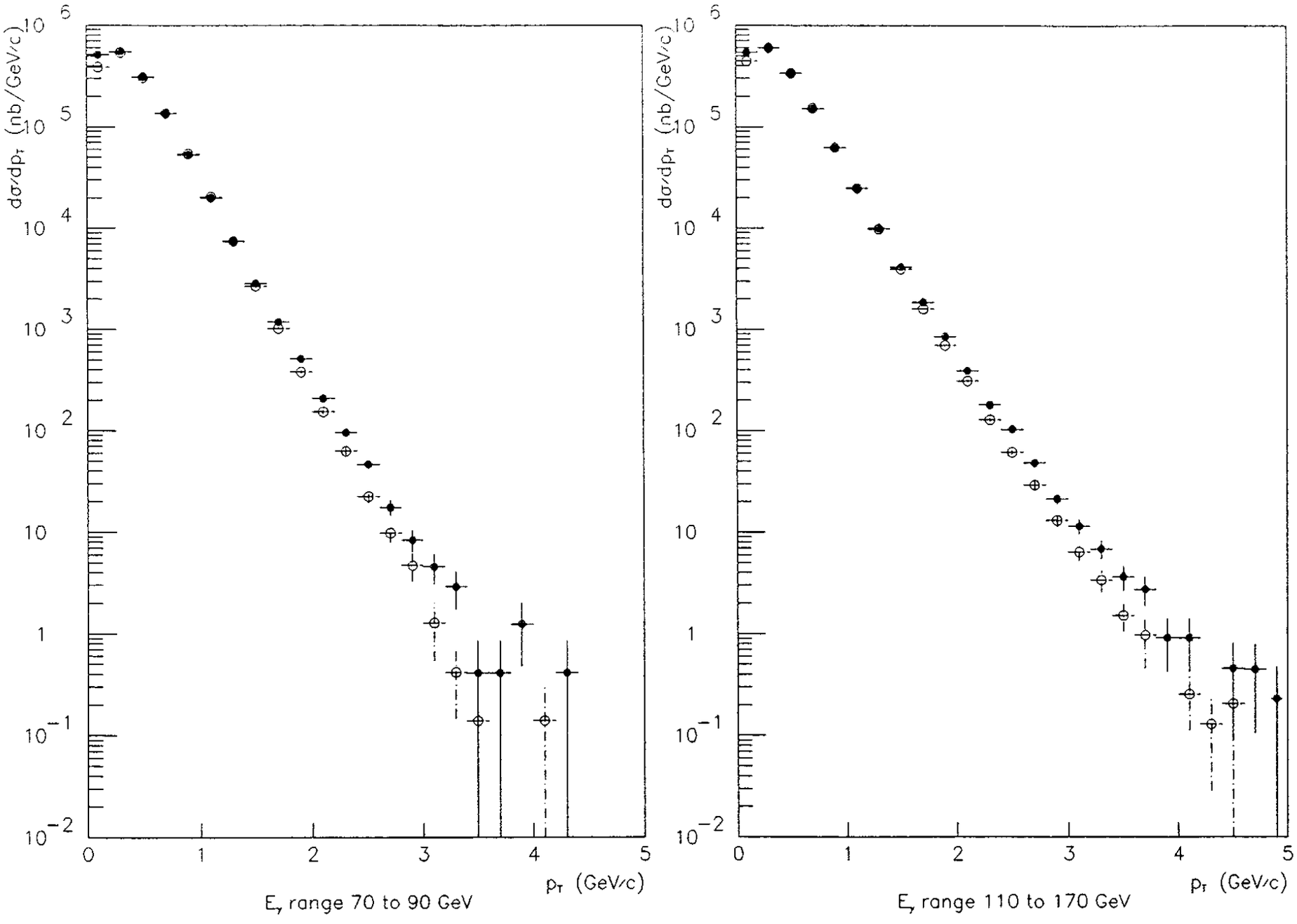
$d\sigma/dp_T$ (nb/GeV/c)
p_T (GeV/c)
E_γ range 70 to 90 GeV
E_γ range 110 to 170 GeV

fig 8

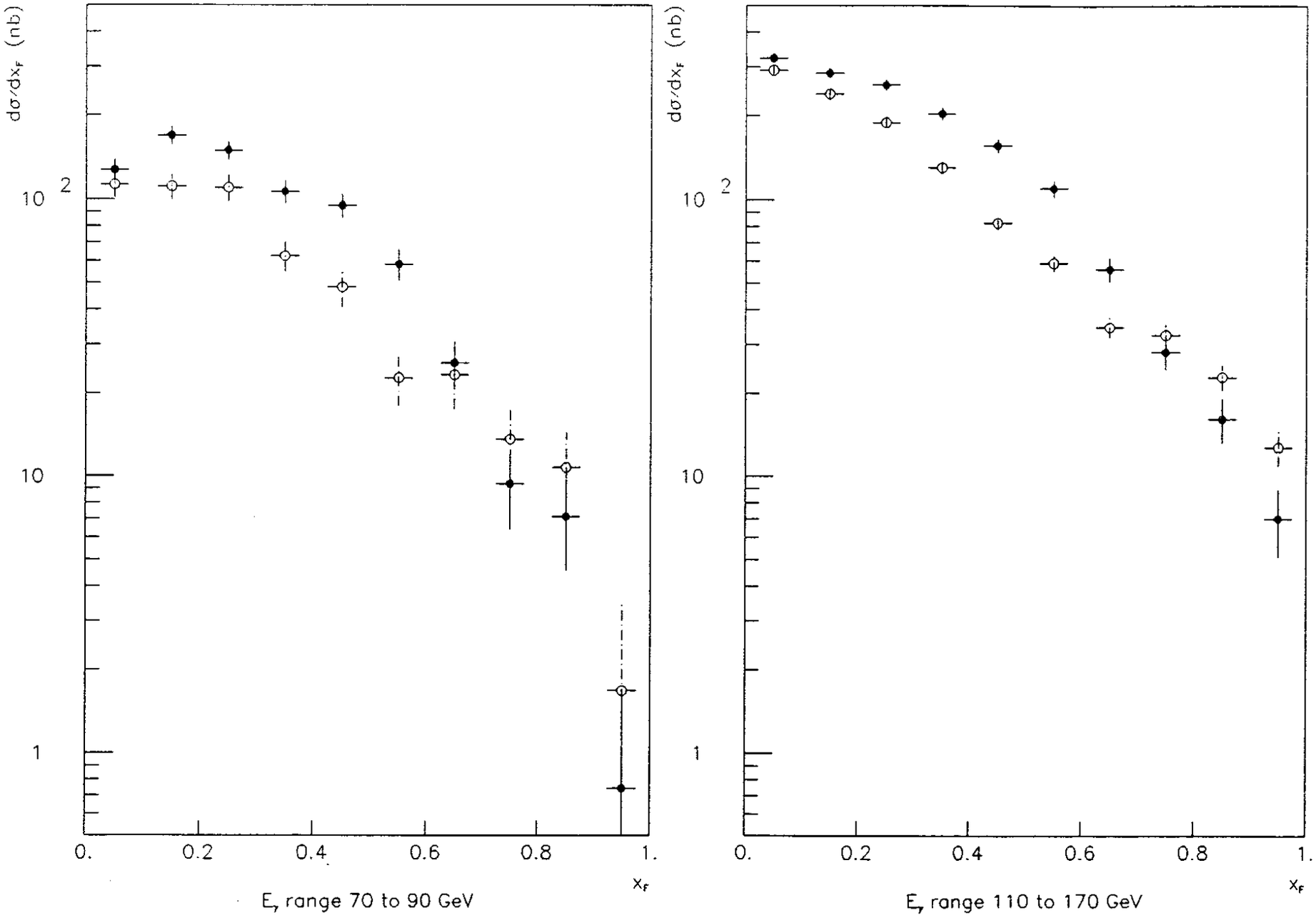
dσ/dx_F (nb)
10 2
10
1
0.
0.2
0.4
0.6
0.8
1.
x_F
E_γ range 70 to 90 GeV
dσ/dx_F (nb)
10 2
10
1
0.
0.2
0.4
0.6
0.8
1.
x_F
E_γ range 110 to 170 GeV

fig 9

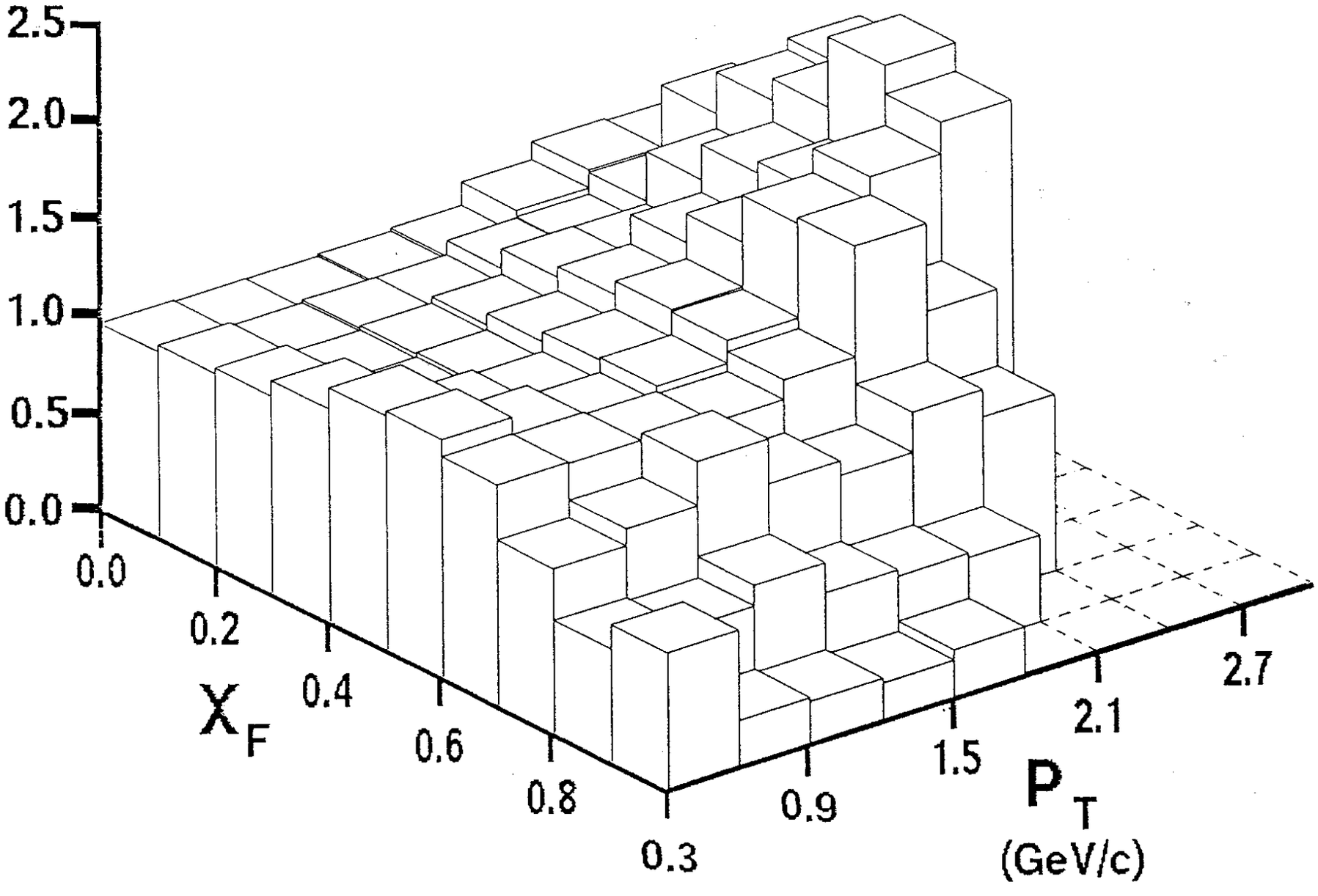

fig 10

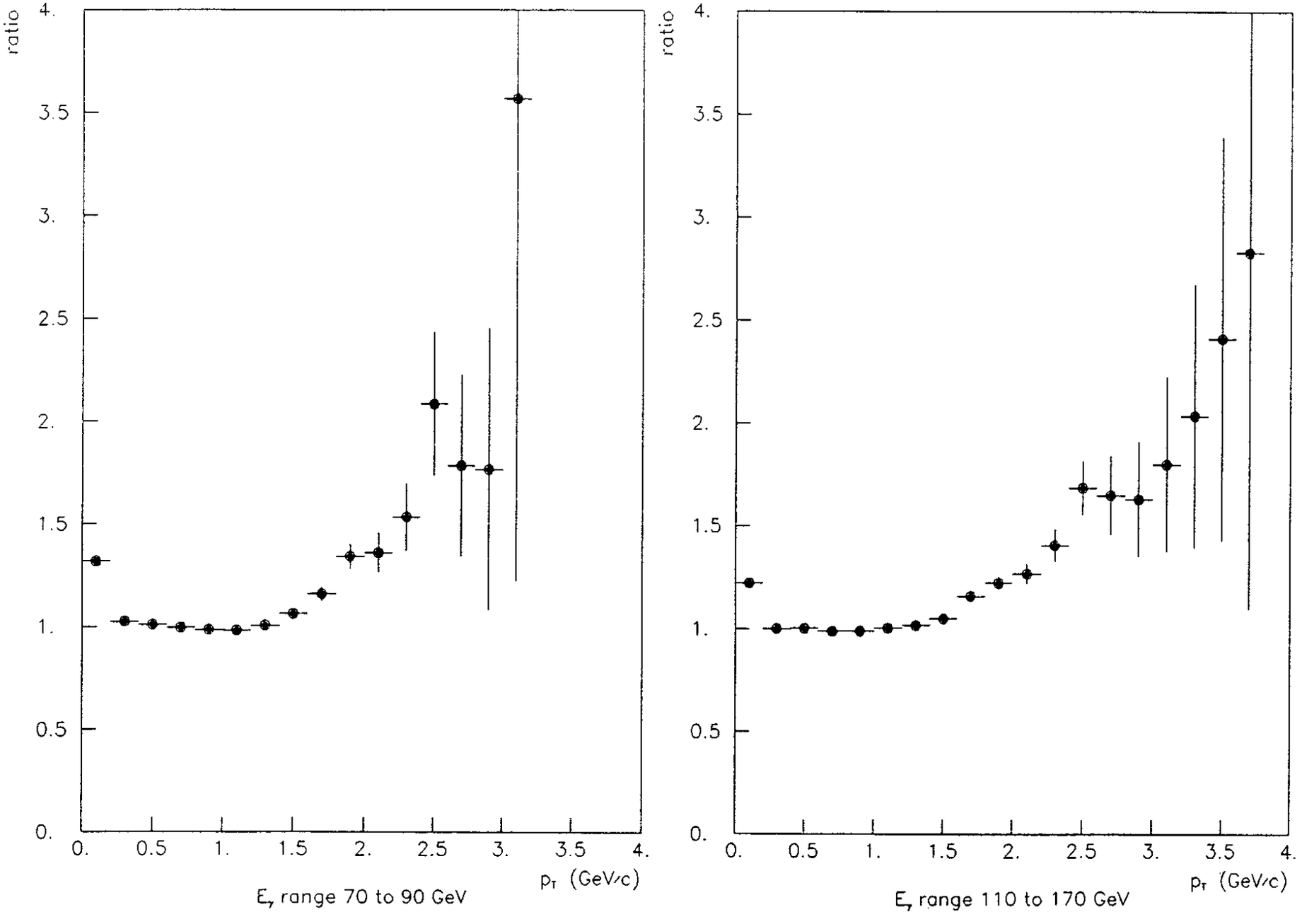
ratio
4.
3.5
3.
2.5
2.
1.5
1.
0.5
0.
0.
0.5
1.
1.5
2.
2.5
3.
3.5
4.
p_T (GeV/c)
E_γ range 70 to 90 GeV
ratio
4.
3.5
3.
2.5
2.
1.5
1.
0.5
0.
0.
0.5
1.
1.5
2.
2.5
3.
3.5
4.
p_T (GeV/c)
E_γ range 110 to 170 GeV

fig 11

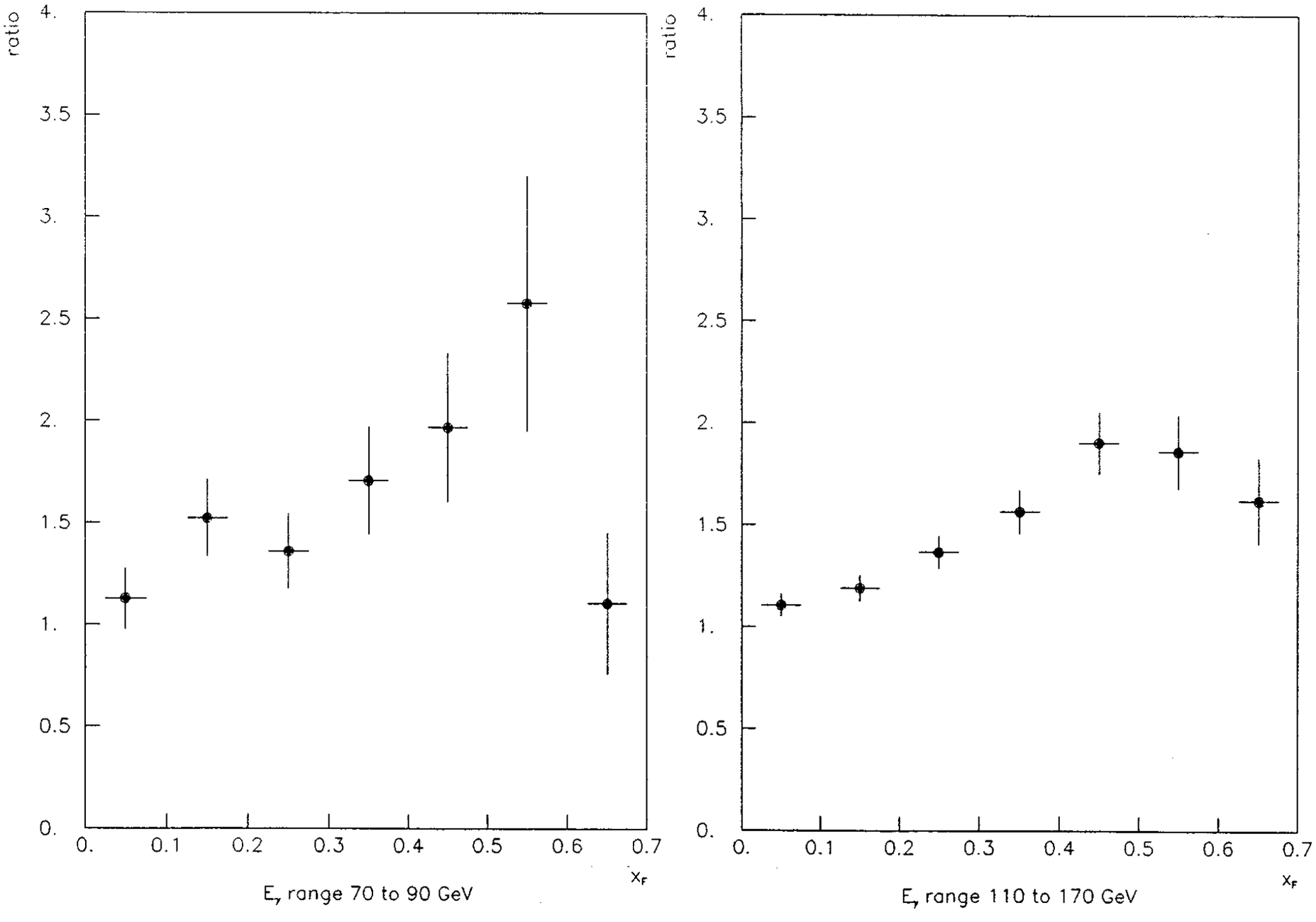
ratio
4.
3.5
3.
2.5
2.
1.5
1.
0.5
0.
0.
0.1
0.2
0.3
0.4
0.5
0.6
0.7
x_F
E_γ range 70 to 90 GeV
ratio
4.
3.5
3.
2.5
2.
1.5
1.
0.5
0.
0.
0.1
0.2
0.3
0.4
0.5
0.6
0.7
x_F
E_γ range 110 to 170 GeV

fig 12

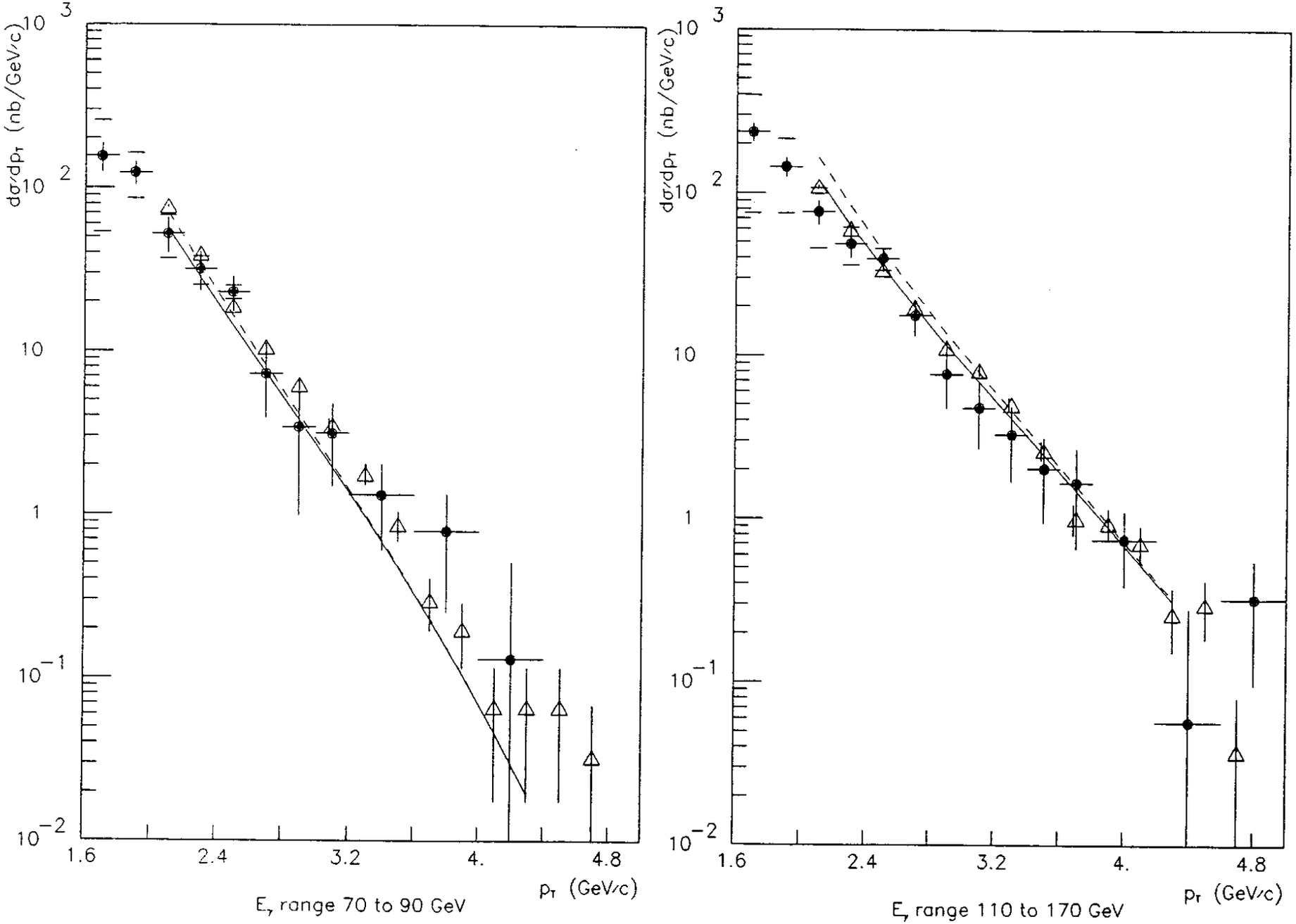
$d\sigma/dp_T$ (nb/GeV/c)
10^3
10^2
10
1
10^{-1}
10^{-2}
1.6
2.4
3.2
4.
4.8
p_T (GeV/c)
E_γ range 70 to 90 GeV
$d\sigma/dp_T$ (nb/GeV/c)
10^3
10^2
10
1
10^{-1}
10^{-2}
1.6
2.4
3.2
4.
4.8
p_T (GeV/c)
E_γ range 110 to 170 GeV

fig 13

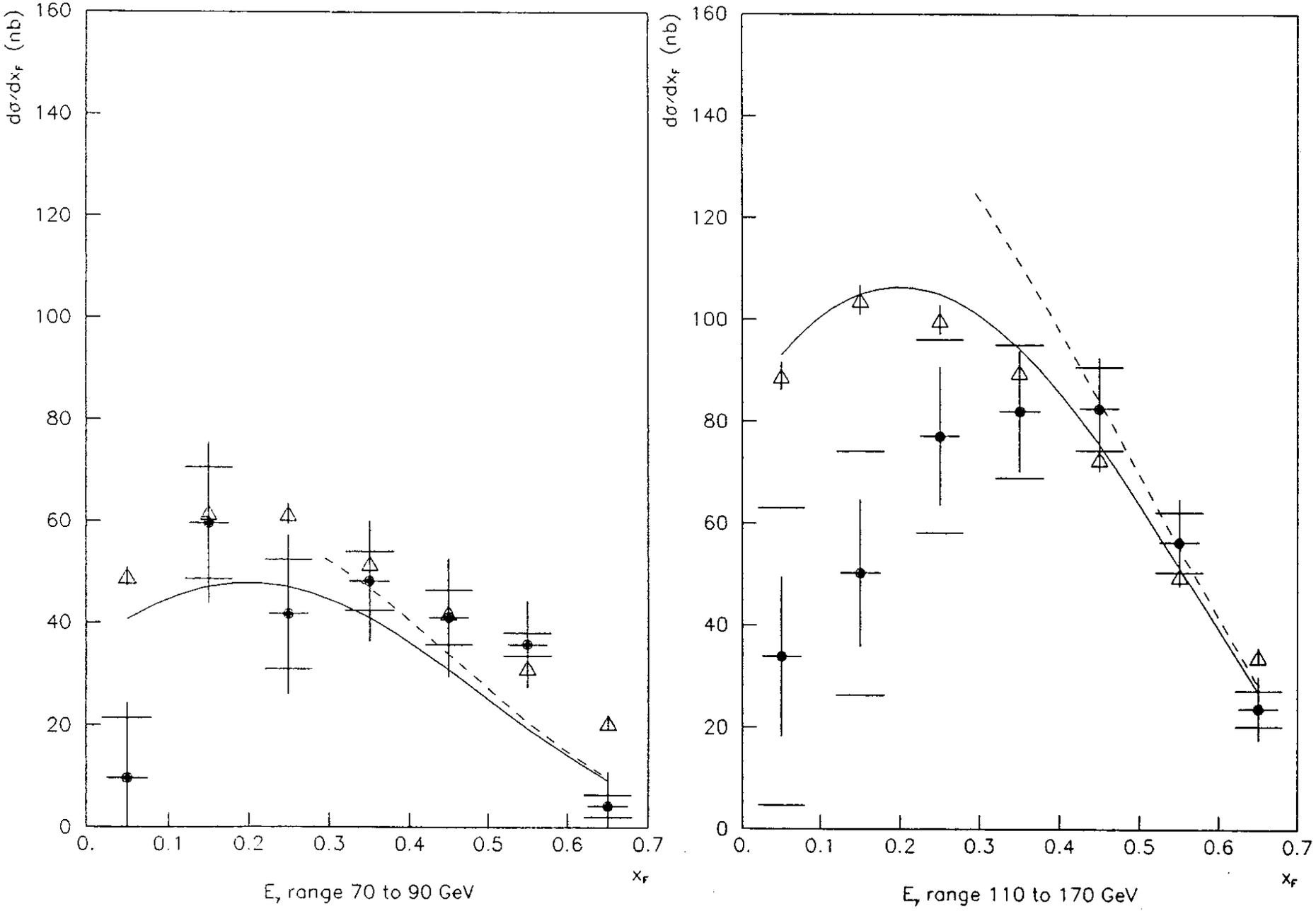
dσ/dx_F (nb)
160
140
120
100
80
60
40
20
0
0.
0.1
0.2
0.3
0.4
0.5
0.6
0.7
x_F
E, range 70 to 90 GeV
dσ/dx_F (nb)
160
140
120
100
80
60
40
20
0
0.
0.1
0.2
0.3
0.4
0.5
0.6
0.7
x_F
E, range 110 to 170 GeV